










## RESEARCH ARTICLE

10.1029/2021GB007270

# Authigenic Formation of Clay Minerals in the Abyssal North Pacific

Zvi Steiner<sup>1</sup> , James W. B. Rae<sup>2</sup> , William M. Berelson<sup>3</sup>, Jess F. Adkins<sup>4</sup>, Yi Hou<sup>3</sup> , Sijia Dong<sup>4</sup> , Giulio I. Lampronti<sup>5</sup>, Xuewu Liu<sup>6</sup>, Eric P. Achterberg<sup>1</sup> , Adam V. Subhas<sup>7</sup> , and Alexandra V. Turchyn<sup>5</sup> 

<sup>1</sup>GEOMAR Helmholtz Centre for Ocean Research Kiel, Kiel, Germany, <sup>2</sup>School of Earth and Environmental Sciences, University of St Andrews, St Andrews, UK, <sup>3</sup>University of Southern California, Los Angeles, CA, USA, <sup>4</sup>Department of Geology and Planetary Sciences, California Institute of Technology, Pasadena, CA, USA, <sup>5</sup>Department of Earth Sciences, University of Cambridge, Cambridge, UK, <sup>6</sup>College of Marine Science, University of South Florida St. Petersburg Campus, St. Petersburg, FL, USA, <sup>7</sup>Department of Chemistry, Woods Hole Oceanographic Institution, Woods Hole, MA, USA

### Key Points:

- North Pacific red clay sediments are a sink for marine calcium, strontium, and potassium
- Authigenic formation of clay minerals is prevalent in pelagic sediments throughout the North Pacific
- The main mechanism for clay formation is recrystallization of aluminosilicates, neof ormation can occur in biogenic silica rich sediments

### Supporting Information:

Supporting Information may be found in the online version of this article.

### Correspondence to:

Z. Steiner,  
zsteiner@geomar.de

### Citation:

Steiner, Z., Rae, J. W. B., Berelson, W. M., Adkins, J. F., Hou, Y., Dong, S., et al. (2022). Authigenic formation of clay minerals in the abyssal North Pacific. *Global Biogeochemical Cycles*, 36, e2021GB007270. <https://doi.org/10.1029/2021GB007270>

Received 13 DEC 2021  
Accepted 27 OCT 2022

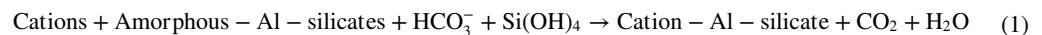
### Author Contributions:

**Conceptualization:** Zvi Steiner, William M. Berelson, Jess F. Adkins  
**Funding acquisition:** Zvi Steiner, Alexandra V. Turchyn  
**Investigation:** Zvi Steiner, James W. B. Rae, William M. Berelson, Yi Hou, Sijia Dong, Giulio I. Lampronti, Xuewu Liu  
**Methodology:** Zvi Steiner  
**Supervision:** Alexandra V. Turchyn  
**Writing – original draft:** Zvi Steiner  
**Writing – review & editing:** James W. B. Rae, William M. Berelson, Jess F. Adkins, Eric P. Achterberg, Adam V. Subhas, Alexandra V. Turchyn

**Abstract** Present estimates of the biogeochemical cycles of calcium, strontium, and potassium in the ocean reveal large imbalances between known input and output fluxes. Using pore fluid, incubation, and solid sediment data from North Pacific multi-corer cores we show that, contrary to the common paradigm, the top centimeters of abyssal sediments can be an active site of authigenic precipitation of clay minerals. In this region, clay authigenesis is the dominant sink for potassium and strontium and consumes nearly all calcium released from benthic dissolution of calcium carbonates. These observations support the idea that clay authigenesis occurring over broad regions of the world ocean may be a major buffer for ocean chemistry on the time scale of the ocean overturning circulation, and key to the long-term stability of Earth's climate.

## 1. Introduction

The balance of elemental inputs and outputs to the ocean determines the chemical composition of seawater, how suitable the ocean is for supporting life, and the partitioning of carbon between the atmosphere, ocean, and marine sediments (Broecker & Peng, 1982). Mackenzie and Garrels (1966a, 1966b) and Sillén (1967) first suggested that authigenic precipitation of clay minerals may play a large role in the oceanic balance of several elements, and termed this process “reverse weathering” (Garrels, 1965; Mackenzie & Garrels, 1966a, 1966b). Recent measurements and modeling work have suggested that authigenic clay mineral formation has played an important role in regulating ocean alkalinity and pH over the course of Earth history (Dunlea et al., 2017; Isson & Planavsky, 2018). The generic reaction that Mackenzie and Garrels (1966a) assigned for reverse weathering is:



The idea of clay authigenesis was overshadowed by the discovery of deep ocean hydrothermal vents, which helped to balance various elemental budgets (Edmond et al., 1979), and the scarcity of evidence to support the widespread presence of authigenic clay formation (Broecker, 1971). However, recent work has highlighted the key role that authigenic clay formation may play in the major ion balance of the ocean over Earth's history (Baronas et al., 2017; Bernhardt et al., 2020; Dunlea et al., 2017; Ehlert et al., 2016; Hazen et al., 2013; Isson & Planavsky, 2018; Isson et al., 2020; Li et al., 2021; Rahman et al., 2017; Siever, 1992; Zhang et al., 2022).

Geochemical data suggest that authigenic precipitation of clay minerals is common in some deep-sea sediments (Baldermann et al., 2015; Baronas et al., 2019; Dunlea et al., 2017; Geilert, Grasse, Doering, et al., 2020; Johnson, 1976; März et al., 2015; Sayles & Bischoff, 1973). Alteration of oceanic crust and volcanic basalts to secondary clay minerals is a prevalent process (Geilert, Grasse, Wallmann, et al., 2020; Santiago Ramos et al., 2020; Staudigel et al., 1981), and stabilization of biogenic silicate frustules by uptake of various metal cations—following the form of Equation 1—forms a key process in their preservation in a variety of open ocean settings (Dixit et al., 2001; Ehlert et al., 2016; Ren et al., 2013; Van Cappellen & Qiu, 1997). Laboratory experiments and use of radiogenic Si isotopes have demonstrated that the chemical reactions during authigenic clay formation can occur rapidly, for example, within 1 year (Dixit et al., 2001; Gaboreau et al., 2020; Loucaides et al., 2010; Michalopoulos & Aller, 1995, 2004; Rahman et al., 2016). Direct observational evidence of authigenic precipitation of clay minerals in surface sediments is, however, currently limited to specific environments,

© 2022. The Authors.

This is an open access article under the terms of the [Creative Commons Attribution License](https://creativecommons.org/licenses/by/4.0/), which permits use, distribution and reproduction in any medium, provided the original work is properly cited.

mainly coastal sediments and river deltas (Michalopoulos & Aller, 1995; Presti & Michalopoulos, 2008; Rahman et al., 2016, 2017). In these environments, detrital sediments carried by tropical rivers provide aluminum and iron that react with biogenic silica and dissolved cations to form new authigenic clay minerals (Michalopoulos & Aller, 2004). Less is understood about authigenic clay formation in red clay sediments, which cover a large portion of the seafloor. With a suitable source of silicic acid ( $\text{Si}(\text{OH})_4$ ), red clay sediments could host vast amounts of authigenic clay formation; given their areal extent, this could have substantial impact on the global elemental balance (Dunlea et al., 2017; Hein et al., 1979; Sayles, 1979; Sun et al., 2016).

Authigenic clay formation may also play an important role in the ocean carbon cycle, via regulation of calcium concentrations, carbonate mineral saturation, and alkalinity. The marine alkalinity balance was a key component of the original argument by Mackenzie and Garrels in favor of a wide spread occurrence of authigenic clay formation in the ocean (Mackenzie & Garrels, 1966b). The main mechanism known to buffer seawater calcium concentration and pH is precipitation and dissolution of  $\text{CaCO}_3$  minerals (Ridgwell & Zeebe, 2005). However, current estimates of the sources and sinks of calcium to the ocean vary by a factor-of-two (Milliman, 1993; Tipper et al., 2010), indicating that we are missing crucial aspects of the marine calcium cycle. An important missing term that explains part of the discrepancy in global budgets of alkalinity and calcium is particulate inorganic carbon (PIC) delivered by rivers (Middelburg et al., 2020). The oceanic cycles of strontium and potassium also appear to be imbalanced, with known inputs to the ocean exceeding the known outputs (Davis et al., 2003; Sun et al., 2016).

Current uncertainties in the marine  $\text{CaCO}_3$  cycle are apparent on large spatial scales, highlighted by discrepancies between budgets of  $\text{CaCO}_3$  production and dissolution that are based on observations of water chemistry and sediment traps. Total alkalinity ( $A_T$ ) and calcium-based estimates of  $\text{CaCO}_3$  dissolution in the North Pacific suggest that a significant portion of carbonate mineral dissolution occurs within the top 2,000 m of the water column, with little signal of dissolution at depth (Feely et al., 2002; Subhas et al., 2022). Sediment trap data from the same region suggest that as much as 20%–30% of the  $\text{CaCO}_3$  export flux reaches a water depth of 5,000 m, with ~25% attenuation in the  $\text{CaCO}_3$  flux between 1,000 and 5,000 m (Honda et al., 2002; Honjo et al., 2008; Timothy et al., 2013). Observed fluxes of settling  $\text{CaCO}_3$  in the North Pacific range from  $120 \pm 40 \mu\text{mol m}^{-2} \text{d}^{-1}$  at 4,000 m near Hawaii (Grabowski et al., 2019) to  $340 \pm 200 \mu\text{mol m}^{-2} \text{d}^{-1}$  at 3,800 m at Ocean Station Papa (Timothy et al., 2013). Despite this apparently large flux of  $\text{CaCO}_3$  to the deep ocean, there is very little  $\text{CaCO}_3$  found in the red clay-dominated sediments of the abyssal North Pacific (Berger, 1970). This is typically attributed to  $\text{CaCO}_3$  dissolution in the deep undersaturated waters (Sulpis et al., 2018). Dissolution of  $200 \mu\text{mol m}^{-2} \text{d}^{-1}$   $\text{CaCO}_3$  at the seafloor, as suggested by the sediment trap data, should release  $150 \text{ mol m}^{-2} A_T$  over 1,000 years. Evenly distributed over the bottom 3,000 m, this would increase  $A_T$  by  $50 \mu\text{mol kg}^{-1}$ . However, complete vertical mixing of this alkalinity signal from benthic dissolution by eddy diffusion is inconsistent with the presence of measurable vertical salinity, temperature, and silicic acid gradients (Hou et al., 2019). The dissolution profile suggested by the sediment trap data thus necessitates a near bottom increase in  $A_T$  and calcium. This is at odds with the lack of a dissolution signal in deep water alkalinity and calcium data (Feely et al., 2002; Steiner et al., 2021).

Here we combine porewater data of calcium, strontium, and potassium concentrations from the North Pacific Ocean, along with sediment data and core-incubation experiments, to explore the removal mechanisms of calcium, strontium, and potassium in abyssal North Pacific sediments. We use our data to systematically assess the nature of chemical interactions occurring across the sediment–bottom-water boundary of the subtropical and subpolar gyre regions, highlighting the important influence of clay authigenesis reactions on global geochemical budgets.

## 2. Materials and Methods

### 2.1. Study Area

Samples were collected at five oceanographic stations during cruise CDisK-IV from Hawaii to Alaska in August 2017 (Figure 1). An 8-barrel multi-corer (Ocean Instruments 800 multi-corer with 9.6 cm inner diameter polycarbonate liners) was used for retrieving short sediment cores and immediately overlying water at each station. Two cores from each multi-corer cast were incubated in a cold room ( $2^\circ\text{C}$ ) over the course of days-to-weeks, two additional cores were sampled in the cold room for porewater using Rhizon samplers, and a fifth core was sectioned for sedimentological work.

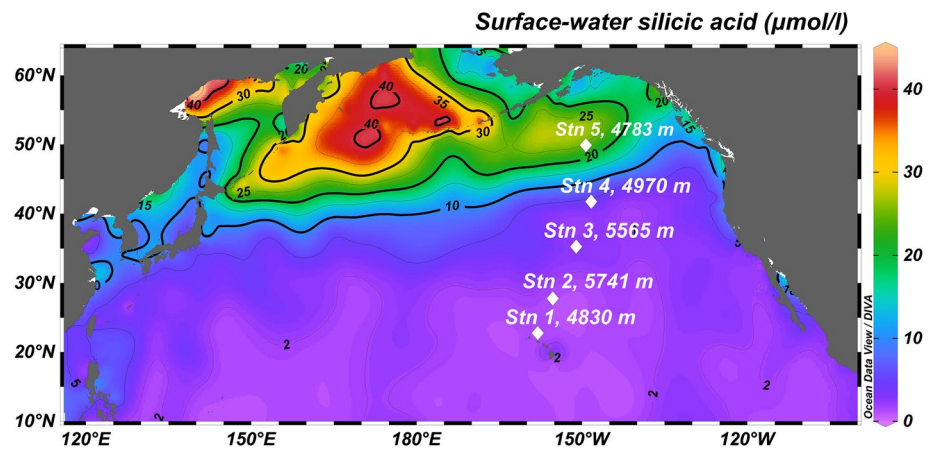


**Figure 1.** Station location and water depth plotted using Ocean Data View version 5.3.0 (Schlitzer, 2020). Surface water silicic acid concentrations are from the World Ocean Atlas 2013 annual data of the years 1955–2012 (<https://odv.awi.de/data/ocean/world-ocean-atlas-2013/>).

The cruise track in the North Pacific Ocean can be broadly divided into two main oceanographic regions, a subtropical gyre and a subpolar gyre. The transition zone in surface water properties that characterize these gyres shifts from 42 in summer to 32°N in winter (Ayers & Lozier, 2010), and is defined by a marked change in *chlorophyll a* concentrations and species composition (Taylor et al., 2018). At time of the CDisK-IV cruise, the transition zone chlorophyll front was located at ~37°N (Hou et al., 2019), hence Stations 1–3 in our data set were within subtropical waters and Stations 4 and 5 in subpolar waters. Calcium carbonate production was dominated by coccolithophorids across the whole transect, with further contributions from foraminifera and pteropods (Dong et al., 2019; Taylor et al., 2018). The subpolar gyre has high fluxes of biogenic silica to the seafloor, 150–1,200 mmol m<sup>-2</sup> y<sup>-1</sup>, due to enhanced supply of nutrients to the surface ocean by deep winter mixing and wind-driven upwelling, resulting in biogenic silica content of ~3% and 4%–8% in sediments from Stations 4 and 5, respectively, compared to 0.5%–1.5% at Stations 1–3 (Honjo et al., 2008; Hou et al., 2019). Higher productivity in the subpolar gyre results in higher seafloor sediment accumulation rate of ~1.5 cm ka<sup>-1</sup> on average, compared with ~0.3 cm ka<sup>-1</sup> for the seafloor underlying the subtropical gyre (Hou et al., 2019; Opdyke & Foster, 1970). Cores from Stations 4 and 5, underlying the subpolar gyre, had clear marks of burrowing organisms in the top 10 cm. At Station 4 the cores also had a “fluff” layer on top of the mud, composed of fresh organic matter and biogenic silica from a diatom bloom that likely settled shortly before core retrieval (Subhas et al., 2020). Visible signs of bioturbation were not observed at Stations 1–3. Manganese nodules were found at the top of the cores from Stations 2–4. Stones of igneous composition, 2–3 cm in diameter were found on top of the Station 5 cores, though the cores were retrieved from the abyssal plain. The main mineral phases in these Station 5 stones, determined using X-ray diffraction (XRD), are quartz, feldspar, plagioclase, and pyroxene.

## 2.2. Porewater Separation

Sediment porewaters were extracted in a cold room, using Rhizon samplers inserted into pre-drilled holes in the core liner, from two cores with undisturbed sediment-water interfaces, from each multi-corer cast. Pre-treatment of the Rhizon samplers and the sampling protocol was different for each of the two cores. One core was sampled with new Rhizon samplers as provided by the manufacturer. A 20 ml syringe was filled from each Rhizon, inserted dry, and the extracted water was filtered again via a 0.45 µm filter (Hou et al., 2019). The second core was sampled using Rhizon samplers that were pre-cleaned with 0.001 N HNO<sub>3</sub> and de-ionized water (18.2 MΩ cm), and soaked in de-ionized water until usage. The first 1 ml was discarded, and 2 ml was then retrieved from each of the samplers (Steiner et al., 2018). There was no measurable difference in the Ca/Na and Sr/Na ratios among the cores. K/Na ratios were systematically lower in the subtropical gyre cores sampled using the acid cleaned Rhizon, but higher in the Station 4 core sampled with the acid cleaned Rhizons. Cation data presented in Figure 5 are the average of the two extractions. Nutrient data were only analyzed in porewater extracted with the non-acid cleaned samplers.

Calculations of the diffusive flux of elements between the sediment and the overlying boundary water can be derived from changes in the elemental concentrations in the porewater, using Fick's first law:

$$J = -\phi \cdot \frac{D_m}{\theta^2} \cdot \left( \frac{dC}{dZ} \right)_0 \quad (2)$$

where  $\phi$  is porosity in the range 0.78–0.89, measured by Hou et al. in the top 1 cm of these cores (Hou et al., 2019) and  $D_m$  is the molecular diffusion coefficient of an element in seawater. Fluxes were calculated based on the slope of porewater element-to-sodium ratios. We also performed these calculations between the bottom-water and the first pore fluid sample assuming a linear gradient over 2 cm. This is a conservative approach, given that the first sampler was, on average, inserted at 1 cm below the sediment interface, and considers the uncertainty concerning where waters drawn by the sampler come from. At 1.5°C, salinity of 35 g kg<sup>-1</sup> and pressure of 600 atm, the molecular diffusion coefficients of potassium, calcium, and strontium are 9.5, 3.5, and 3.5 · 10<sup>-6</sup> cm<sup>2</sup> s<sup>-1</sup>, respectively (Li & Gregory, 1974). Tortuosity ( $\theta$ ) corrections are made by assuming the relationship  $\theta^2 = 1 - \ln(\phi^2)$  (Boudreau, 1997). As discussed below, the assumption that the pore water profile is unaffected by recovery is a critical assumption, and likely not always true (Glud et al., 1994).

### 2.3. Incubation Experiments

Duplicate cores from each station were incubated in a cold room (2°C) for 6–14 days to provide constraints on elemental fluxes to and from the seafloor. Five to seven samples were collected during the incubation period. The incubation setup is described in detail in (Hammond et al., 2004; Hou et al., 2019). Briefly, an incubation cap was inserted into each core, and the water level adjusted to ~12 cm above the sediment surface. A 12 V motor in the incubation cap stirred the overlying water at 30 rpm. Nitrate concentrations in the overlying water increased throughout the incubations, indicating that oxic conditions were maintained. Samples were filtered through 0.45 μm PES filters. Each sampling lowered the water level by ~0.6 cm.

Elemental fluxes from sediment porewater to bottom-water can be calculated from the core incubations using the following relationship:

$$J = \frac{\Delta C \cdot V}{A \cdot \Delta t} = \frac{\Delta C}{\sum(\Delta t_i / h_i)} \quad (3)$$

where  $\Delta C$  is the change in overlying water concentrations during time elapsed  $\Delta t$ ,  $V$  is the volume of overlying water,  $A$  is surface area of the sediment, and  $h_i$  is the height of the overlying water column at  $t_i$ . When element concentrations are plotted versus the sum of time elapsed divided by the height of the overlying water in the incubated core, the slope of these correlations yields the flux  $J$  (in mol m<sup>-2</sup> time<sup>-1</sup>). We use this formulation because the height of the water column in each core changed with each sample drawn ( $V = f(t)$ ).

### 2.4. Water Chemistry

#### 2.4.1. Major Element Concentrations

The concentrations of calcium, strontium, potassium, magnesium, lithium, and sodium were analyzed at the University of Cambridge with an Agilent Technologies 5100 ICP-OES, using the method developed by Schrag (1999) and modified by Steiner et al. (2020). Samples were diluted by a factor of ~80 to a common salinity with 0.16 M HNO<sub>3</sub>, and analyzed in duplicate, using sample-standard bracketing to correct for instrumental drift. The bracketing standard was IAPSO seawater calibrated for absolute concentrations of calcium and strontium by isotope dilution Thermal Ionization Mass Spectrometer (TIMS) (Steiner et al., 2020). Lithium concentrations in the IAPSO standard were determined using a Varian 720 ICP-OES at GEOMAR Helmholtz Centre for Ocean Research Kiel, by standard additions of LiCl (99.999%, Roth). To verify that no uncorrected drift remained in the data, the samples were analyzed in a random order rather than following their depth/location order. Element concentrations were determined using the Ca317.993, Ca422.673, Mg279.078, Mg285.213, Sr421.552, Li670.783, Na568.821, and Na589.592 nm wavelengths, as the element to sodium ratios. The analysis of element ratios rather than direct analyses of the concentrations of individual elements takes advantage of the simultaneous analyses of all wavelengths by the ICP-OES, and corrects for measurement errors induced by plasma instability. Element concentrations, normalized to constant absolute TEOS-10 salinity of 35 g kg<sup>-1</sup> were calculated from the element-to-sodium

ratios for the incubation samples based on the assumption of constant sodium-to-salinity ratios, an assumption that underpins conductivity-based measurements of seawater salinity (IOC et al., 2010; Millero et al., 2008). A constant sodium-to-salinity ratio is not a valid assumption for porewater (Sayles, 1979), hence the porewater data are reported as the element-to-sodium ratios. Deep-sea drilling data from the Northeast Pacific suggest constant sodium concentrations with depth in the cores (Manheim et al., 1970), and sodium concentrations in seawater are ~50 times the concentrations of potassium and calcium, requiring much larger changes in sodium concentrations to produce the same variations, therefore variations in element-to-sodium ratios in the porewater data presented here are assumed to represent variations in the concentration of the numerator.

#### 2.4.2. Nutrients

Nutrient samples were filtered using Acrodisc syringe filters with a nominal pore size of 0.4  $\mu\text{m}$  and kept frozen at  $-18^{\circ}\text{C}$  until analyses. The concentrations of soluble reactive phosphorous and total oxidized nitrogen (nitrate + nitrite) were analyzed at the U. Maryland Nutrient Analytical Services Lab (Salomons, MD, USA).

#### 2.4.3. Calcium Isotopes

Samples for calcium isotope analysis were spiked with a  $^{42}\text{Ca}$ - $^{48}\text{Ca}$  double spike at a 10:1 sample to spike ratio. Calcium was separated from the seawater matrix using a Dionex ICS 5000+ ion chromatograph with a fraction collector, and calcium isotope ratios were analyzed using a Triton Plus Multi-collector TIMS, following the method described in Bradbury and Turchyn (2018). Each Triton run consisted of 21 samples—15 unknown samples, an IAPSO standard from batch P157, and five NIST915B standards. Instrument mass bias was corrected in each run to  $915\text{b }^{44/40}\text{Ca} = -0.28\text{‰}$  on the Bulk Silicate Earth (BSE) scale. The long-term average of the IAPSO runs is  $\delta^{44}\text{Ca}_{\text{BSE}} = 0.855 \pm 0.024\text{‰}$  (1 SE,  $n = 11$ ). Most samples presented in this work were analyzed in duplicate, which were typically analyzed during different TIMS sessions. The average difference between full procedural duplicates was 0.044‰.

### 2.5. Solid Sediments

#### 2.5.1. Particulate Inorganic Carbon

Sediment PIC concentration profiles were determined from dried and ground sediment powder. Splits were weighed into 10 mL exetainer test tubes (5–20 mg) and acidified with 10% phosphoric acid. The evolved  $\text{CO}_2$  was measured using a Picarro 2131i. Total  $\text{CO}_2$  in the Picarro analysis was standardized by running known masses of optical grade calcite standard material.

#### 2.5.2. Particle Size Analyses

Particle size distributions were analyzed by laser using a Malvern Instruments Mastersizer 2000. Samples were treated with 30%  $\text{H}_2\text{O}_2$  for 24 hr at room temperature and 1 hr at  $80^{\circ}\text{C}$  to remove organic matter. The samples were then centrifuged at 3,000 rpm for 5 min and the  $\text{H}_2\text{O}_2$  was decanted. 4.4% sodium hexametaphosphate was added to the samples as dispersant, the samples were vortexed and left overnight. The samples were vortexed again immediately before analyses and analyzed 3–6 times for their grain size distribution.

#### 2.5.3. XRD

The clay fraction was separated from the bulk sediment by inserting several hundred milligrams of sediment into 50 mL centrifuge tubes filled with double distilled water to the 25 mL mark. The tubes were vortexed and settled. After 30 min, 1 mL of the water sample was pipetted from a depth of 2–2.2 cm below the water surface and dehydrated on a silicon slab. X-ray powder diffraction data of the clay fraction of the sediments were collected in Bragg-Brentano geometry on a D8 Bruker diffractometer equipped with a  $\text{Cu K}\alpha$  primary beam and a Vantec position sensitive detector. Collection conditions were:  $3\text{--}60^{\circ}$  in  $2\theta$ ,  $0.04^{\circ}$  step size, 2.4 s/step, divergence slits 0.2 mm. Rietveld refinements were performed with the software TOPAS V6 (Coelho, 2018).

A shifted Chebyshev function with 3–6 parameters was used to fit the background. Peak shape was modeled using a Pseudo-Voigt function. Instrumental parameters and the instrumental contribution to peak broadening were modeled by refining data collected on a LaB6 660b NIST standard using a fundamental parameters approach, while the crystal size contribution to peak broadening was modeled with one single Gaussian parameter per each phase. The crystal size was estimated by whole pattern Rietveld refinements by including the Scherrer equation in the peak shape function,



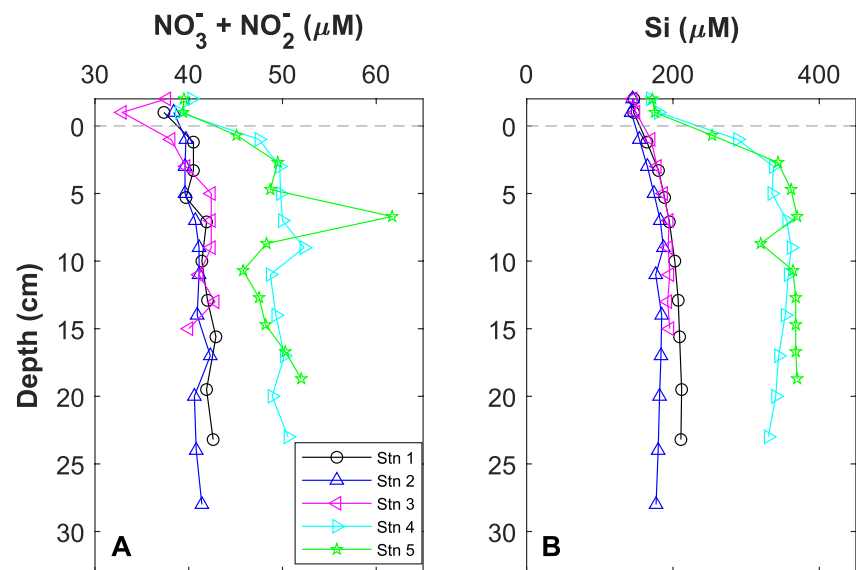


**Figure 2.** Porewater profiles of nitrate + nitrite, and silicic acid in the five studied stations. Overlying water concentrations are drawn at arbitrary depth of 1 cm above the sediment-water interface. Silicic acid data are from Hou et al. (2019). Nutrient samples from the deepest Niskin bottle retrieved at the same stations, ~50 m above the seafloor, are shown on the upper x-axis.

$$\text{crystalsize [in nm]} = k \lambda / (10 \cdot \Delta\theta \cdot \cos \theta) \quad (4)$$

where  $k$  is a crystal shape factor, most often assumed to be 0.9,  $\lambda$  is the radiation wavelength, and  $\theta$  is the diffraction angle, into the peak shape function in a given crystallographic direction ( $hkl$ ) according to the following equation:

$$\text{fwhm}(2\theta, hkl) = (180/\pi) \lambda / (\cos \theta \cdot \text{crystal size}) \quad (5)$$

where  $\text{fwhm}(2\theta)$  is the full width at half maximum of the peak at a given diffraction angle and a given crystallographic direction. Crystal structures were retrieved from the ICSD database (Allmann & Hinek, 2007) (ICSD entry codes: 63192, kaolinite; 161171, montmorillonite; and 90144, illite). No structural parameter was refined other than unit cell parameters.

#### 2.5.4. SEM-EDS

Sediment samples were imaged with a Quanta-650F scanning electron microscope and their chemistry analyzed with energy dispersive X-ray spectroscopy using two XFlash 6/30 Bruker detectors at the University of Cambridge. The samples were prepared as smear slides by diluting 200  $\mu\text{L}$  sediment in 25 mL double distilled water. Each sample was vortexed, a few drops were dispensed on a glass slab and dehydrated. Samples were coated with carbon prior to analyses.

### 3. Results and Discussion

#### 3.1. Porewater Nutrients

Concentrations of nitrate + nitrite increase in the porewater of the first cm relative to bottom water concentrations and remain high over the depth range sampled (Figure 2a). The absence of a decrease in nitrate + nitrite indicates that aerobic remineralization of organic matter prevails in the top 30 cm at all five stations. Oxidation of organic matter and ammonium by oxygen releases protons to the water (Froelich et al., 1979), hence the porewater should become even more corrosive to calcite than the bottom waters of the North Pacific. Porewater silicic acid concentrations also increase over the top seven cm, likely due to dissolution of biogenic silica (Figure 2b, Hou et al., 2019). At Station 4, dissolved silicic acid concentrations decrease below 10 cm. Stations 4 and 5 receive higher fluxes of organic matter and biogenic silica than Stations 1–3, and this is reflected by the elevated porewater

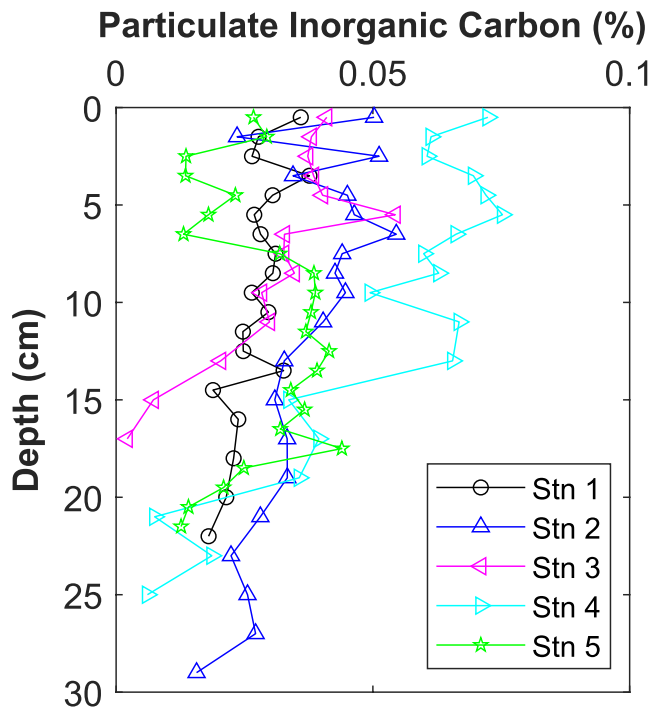


Figure 3. Particulate inorganic carbon content of the studied sediment cores.

concentrations of nitrate + nitrite and silicic acid. Porewater concentrations of silicic acid are distinctly below saturation with respect to opal at all sites despite the abundant presence of biogenic silica in the sediments.

### 3.2. Alkaline Earth Metal Fluxes Across the Sediment-Water Interface

An inferred calcium flux at the sediment surface can be calculated from the delivery of  $\text{CaCO}_3$  to the seafloor. Sediment trap data suggest a flux of  $120\text{--}340 \mu\text{mol CaCO}_3 \text{ m}^{-2} \text{ d}^{-1}$  to the North Pacific seafloor (Grabowski et al., 2019; Honda et al., 2002; Timothy et al., 2013). In the absence of bottom-water and benthic dissolution, and assuming  $\text{CaCO}_3$  density of  $2,710 \text{ kg m}^{-3}$  and porosity of 0.7, a  $\text{CaCO}_3$  flux of  $120 \mu\text{mol m}^{-2} \text{ d}^{-1}$  translates to a sediment accumulation rate of  $0.5 \text{ cm ka}^{-1}$ , which is almost double the average accumulation rate of sediments underlying the subtropical gyre (Opdyke & Foster, 1970). Given the very low PIC content of these deep Pacific sediments ( $<0.1\%$ , Figure 3), we should expect a similar calcium flux out of the sediment into the water column. However, our incubation data do not show any change in the calcium concentrations over the incubation period (Figure 4a). Indeed, the lower porewater calcium concentrations compared to overlying bottom-waters suggest that abyssal North Pacific sediments are in fact a sink for calcium in the subtropical gyre (Figure 5a).

We analyzed the calcium isotope composition of porewaters from Stations 2 and 4 as an additional constraint on the location and nature of the reactions consuming calcium in these sediments (Figure 6). The top 30 cm of the sediment column is open to exchange with seawater on the time scale of years

to decades ( $t = z^2 / \frac{\phi \cdot 2D_m}{\theta^2} = (30\text{cm}^2 / \frac{0.6 \cdot 1 \cdot 10^{-5}}{1 - \ln 0.6^2}) \sim 10\text{years}$ ). In contrast, sediments accumulate over thousands of years. The porewater chemistry thus represents the modern ocean and not conditions at time of sediment accumulation. Therefore, all samples should have the same composition as the bottom water, unless chemical reactions such as precipitation, adsorption, dissolution or recrystallization are occurring on a timescale faster than diffusion. Precipitation of  $\text{CaCO}_3$  preferentially consumes the light  $^{40}\text{Ca}$  isotope, leaving seawater more enriched in  $^{44}\text{Ca}$  (Fantle & Tipper, 2014). Adsorption of calcium to clay surfaces and precipitation of non-carbonate, calcium-bearing minerals, are also expected to enrich the residual solution in heavier calcium isotopes (Brazier et al., 2019; Ockert et al., 2013). In contrast, dissolution of  $\text{CaCO}_3$  decreases the  $\delta^{44}\text{Ca}$  signature of the porewater calcium.

All porewater samples analyzed here show  $\delta^{44}\text{Ca}$  that are equal to or higher than the bottom water  $\delta^{44}\text{Ca}$ . These analyses suggest that calcium is removed from porewater both at Station 2, where porewater  $\text{Ca}/\text{Na}$  ratios decrease with depth in the sediment, as well as at Station 4, where porewater  $\text{Ca}/\text{Na}$  ratios do not decrease with depth. The calcium isotope data thus suggest that the process responsible for calcium uptake is active in the top portion

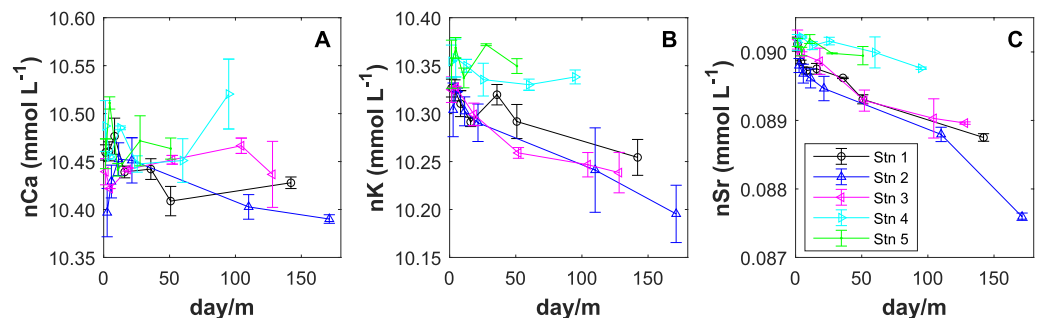
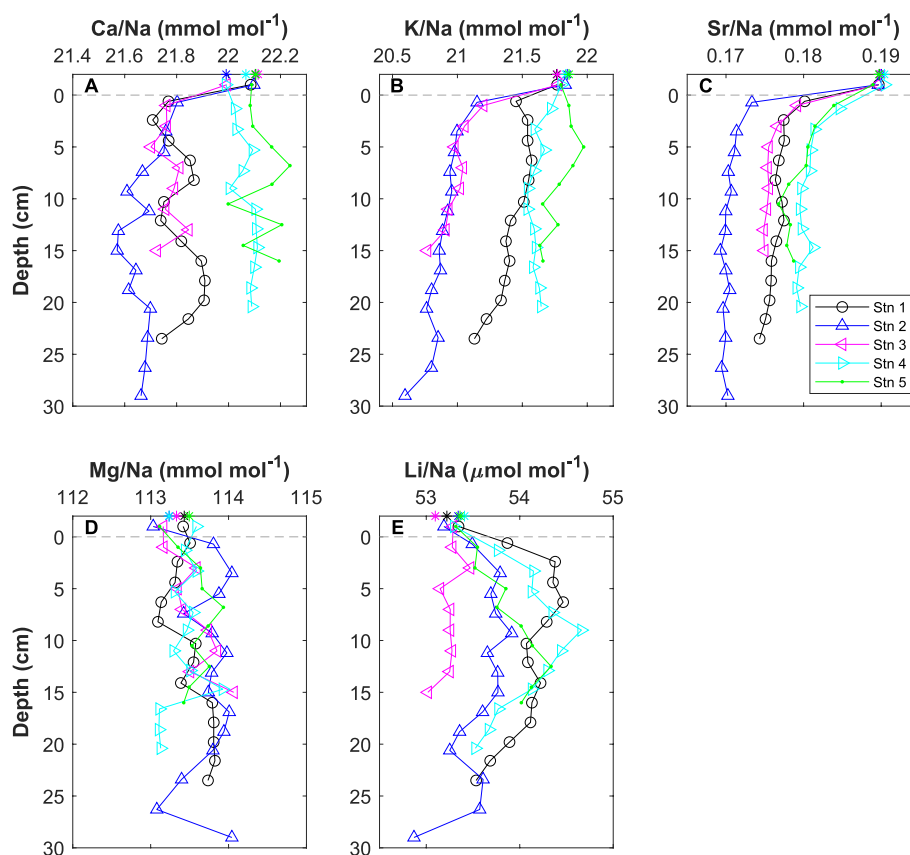


Figure 4. Calcium, potassium, and strontium, normalized to absolute salinity of  $35 \text{ g kg}^{-1}$ , in the overlying water over the course of several days incubations. The x-axis units are the ratio of time-to-water-height in the incubation tube, calculated for each sample interval to correct for curvature in the concentration gradient that results from changes of the incubation water level. Error bars mark the difference between concentrations measured in duplicate cores.



**Figure 5.** Porewater profiles of cores retrieved from Stations 1–5. Each profile shows averaged element-to-sodium ratios in water from two cores from the same multi-corer cast. Based on the difference between duplicate cores,  $1\sigma$  SD for Ca/Na, K/Na, Sr/Na, Mg/Na, and Li/Na ratios in units of  $\text{mmol mol}^{-1}$  are 0.056 (0.26%), 0.157 (0.74%), 0.00047 (0.26%), 0.33 (0.29%), and 0.00020 (0.37%), respectively. Overlying water concentrations are placed at arbitrary depth of 1 cm above the sediment-water interface. Asterisks on the upper x-axis are the concentrations in water samples from the deepest Niskin bottle retrieved at the same stations,  $\sim 50$  m above the seafloor.

of sediments beneath both the subtropical and subpolar gyres. The element-to-sodium data from Stations 1–3 suggest that the reactions consuming calcium, strontium, and potassium mostly occur in the uppermost sediment, while the calcium isotope data suggest it occurs a few cm deeper. This disagreement suggests that calcium uptake is a two-step process, initially involving faster calcium uptake with a small calcium isotope fractionation factor, followed by a second, slower reaction, with a larger calcium isotope fractionation factor. The first reaction could be adsorption to mineral surfaces or precipitation of amorphous calcium bearing phases, and the second reaction may be consistent with recrystallization of the initial phase to thermodynamically stable minerals. Authigenic  $\text{CaCO}_3$  precipitation is an unlikely cause of calcium removal from sedimentary pore fluids because of the extremely low %PIC in these sediments ( $>0.1\%$ , Figure 3), which are decreasing with depth, as well as the general undersaturation of the North Pacific bottom waters with respect to calcite and aragonite (Figure S1 in Supporting Information S1). Under the prevailing bottom water conditions, authigenic precipitation of  $\text{CaCO}_3$  requires a substantial source of alkalinity; the absence of a decrease in porewater nitrate concentrations suggests that within the depth range sampled, the sediments are aerobic, implying that remineralization of organic matter further decreases porewater pH and calcite saturation state (Figure 2, Soetaert et al., 2007).

It is important to consider whether sampling artifacts account for at least part of the obtained results. Artifacts in measured strontium, calcium, and potassium concentrations may be related to de-pressurization, temperature changes or porewater extraction. For example, pressure changes during core retrieval shift the equilibrium solubilities of the carbonate system. However, a pressure effect should have affected the results as a function of water depth, but such a trend is not observed here; Station 1 cores were retrieved from similar depths to Stations 4 and 5 and show different trends. Core warming during retrieval can modify equilibrium constants and



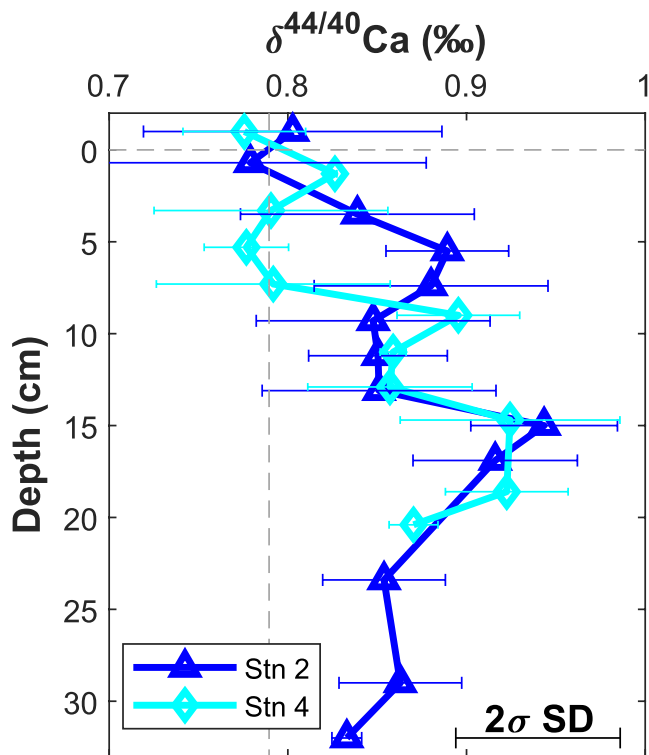


**Figure 6.** Porewater calcium isotopic composition in Stations 2 and 4.  $\delta^{44}\text{Ca}$  is reported on the bulk silicate Earth scale.  $1\sigma$  SD is 0.046, based on 17 full procedural replicates. An IAPSO seawater standard was analyzed alongside the samples and gave an average  $\delta^{44}\text{Ca} = 0.85 \pm 0.04$  ( $2\sigma$  SE,  $n = 5$ ). Horizontal error bars mark the standard errors of replicate analyses of individual samples.  $\delta^{44}\text{Ca}$  of the overlying waters is marked at 1 cm above the sediment–water interface. The horizontal dashed line marks the sediment–bottom-water interface, the vertical dashed line marks the average  $\delta^{44}\text{Ca}$  of the two overlying water samples.

the saturation state of various minerals, particularly in the warmer surface waters of the subtropical gyre. It has previously been shown that core warming during retrieval and porewater extraction can significantly increase the apparent porewater potassium concentrations (Mangelsdorf et al., 1969), but this is opposite to the decreased potassium concentrations we observe, and our core handling was done in a cold room under bottom-water temperature conditions. However, the fluxes of potassium calculated from the interface gradient are unrealistically high compared to the residence time of potassium in the ocean, suggesting the possibility that physical extraction of the porewaters creates an artificial difference between the porewater and bottom-water element concentrations. Therefore, we consider the K/Na porewater concentration gradient as a more reliable approach to calculate potassium fluxes in these samples. Precipitation of  $\text{CaCO}_3$  during retrieval of carbonate rich deep-sea cores due to pressure decrease has been previously shown to be a problem (Emerson et al., 1982). The combined effect of core warming and depressurizing during retrieval increases the average  $\Omega_{\text{calcite}}$  (calcite saturation state) of the water overlying the core from 0.6 to 2. It has been previously shown that heterogeneous precipitation of  $\text{CaCO}_3$  from supersaturated seawater can occur, but on the timescales of hours-to-days this has only been documented in the presence of  $\text{CaCO}_3$  seed minerals and at  $\Omega_{\text{calcite}} > 3$  (Wurgaft et al., 2016). The PIC contents that we measured in the cores are  $< 0.1\%$  in all cores and depths (Figure 3), hence both conditions for heterogeneous precipitation are not met here. In addition, porewater extraction using Rhizon samplers was previously shown to promote  $\text{CaCO}_3$  precipitation in  $\text{CaCO}_3$  rich-sediments during sampling due to outgassing of  $\text{CO}_2$  (Schrum et al., 2012; Steiner et al., 2018). This effect is also unlikely to be of importance here because of the low carbonate content of the sediment.

The sedimentary sink for calcium is unlikely to be authigenic precipitation of  $\text{CaCO}_3$  since there is little  $\text{CaCO}_3$  in these sediments that underlie bottom waters that are themselves highly undersaturated with respect to calcite ( $\Omega_{\text{calcite}} < 0.7$ , Figure 3 and Figure S1 in Supporting Information S1). Interface sediments are more reactive since they formed in different environments and had less time to chemically equilibrate with seawater. It is possible that reaction timescales are sufficiently fast to stabilize these mineral phases before they are buried.

A non-carbonate sink for calcium would likely also be a sink for other cations. Our incubation and porewater data suggest that the sediments underneath the North Pacific subtropical gyre are a relatively larger sink for strontium and potassium than calcium (Figures 4 and 5, Table 1). Excess uptake of potassium and strontium

**Table 1**  
Calculated Fluxes Across the Sediment–Bottom-Water Interface Based on the Porewater and Incubation Data

Station	Porosity <sup>a</sup>	Porewater interface fluxes <sup>b</sup> ( $\mu\text{mol m}^{-2} \text{day}^{-1}$ )			Porewater gradient fluxes <sup>c</sup> ( $\mu\text{mol m}^{-2} \text{day}^{-1}$ )			Incubation fluxes ( $\mu\text{mol m}^{-2} \text{day}^{-1}$ )		
	0–1 cm	Ca	Sr	K	Ca	Sr	K	Ca	Sr	K
1	0.865	$-160 \pm 40$	$-4.8 \pm 0.3$	$-420 \pm 410$	$4.0 \pm 2.6$	$-0.17 \pm 0.03$	$-41 \pm 7$	$-280 \pm 1,700$	$-8.7 \pm 1.2$	$-460 \pm 140$
2	0.823	$-130 \pm 30$	$-7.2 \pm 0.6$	$-790 \pm 290$	$-3.3 \pm 2.1$	$-0.08 \pm 0.03$	$-36 \pm 5$	$-260 \pm 1,300$	$-12.0 \pm 1.4$	$-710 \pm 140$
3	0.855	$-110 \pm 50$	$-5.1 \pm 0.9$	$-740 \pm 120$	$1.8 \pm 3.9$	$-0.24 \pm 0.07$	$-62 \pm 13$	$+250 \pm 2,600$	$-11.0 \pm 2.0$	$-810 \pm 210$
4	0.877	$+20 \pm 40$	$-3.1 \pm 0.9$	$-110 \pm 50$	$3.7 \pm 1.6$	$-0.18 \pm 0.06$	$-6 \pm 7$	$+330 \pm 3,000$	$-4.2 \pm 1.5$	$-220 \pm 220$
5	0.784	$-0 \pm 30$	$-2.0 \pm 0.6$	$+60 \pm 60$	$1.5 \pm 5.8$	$-0.35 \pm 0.09$	$-50 \pm 13$	$-210 \pm 5,980$	$-3.8 \pm 2.8$	$-0 \pm 510$

Note. Negative values stand for fluxes into the sediment.

<sup>a</sup>Porosity in the top cm of the sediment, after Hou et al. (2019). <sup>b</sup>Calculated from the concentration difference between the core overlying water and top Rhizon. <sup>c</sup>Calculated from linear extrapolation of the porewater gradient, ignoring overlying water data.

over calcium suggests that the sedimentary sink for calcium is authigenic clay mineral precipitation (Hindshaw et al., 2013; Michalopoulos & Aller, 1995) and not authigenic carbonate mineral precipitation. Magnesium is also often associated with clay minerals, and limited variability in measured magnesium concentrations (Figure 5d) may be related to analytical challenges, as it is harder to observe changes in magnesium concentrations against its high background concentration. Limited variability in magnesium concentrations is also consistent with observations that the complete dissolution of primary mineral phases and concurrent growth of secondary clays in low-temperature alteration of oceanic crust does not necessarily change the magnesium content of the bulk solids (Santiago Ramos et al., 2020). The data suggest that there is a slight increase in porewater magnesium concentration with depth, which is consistent with dissolution of magnesium-rich detrital minerals.

Further evidence for sedimentary dissolution and crystallization of aluminosilicate minerals is found in the Li/Na data (Figure 5e). In four of the five stations, Li/Na ratios increase in the top sediment layers and decrease back to seawater concentrations at depth. Lithium is a proxy for the inorganic silicate cycle since it is found in low concentrations in organic matter,  $\text{CaCO}_3$  and biogenic silica but can readily replace  $\text{Mg}^{2+}$ ,  $\text{Fe}^{2+}$ , and  $\text{Al}^{3+}$  in the crystals of aluminosilicate minerals (Hindshaw et al., 2019; Martin et al., 1991). There are nearly 18,000 mols of sodium for each mol of lithium in seawater, making it unlikely that adsorption can be responsible for the deep decrease in Li/Na since sodium should outcompete lithium for adsorption sites under these conditions (Hindshaw et al., 2019). The lithium profiles thus hint at net dissolution of aluminosilicate minerals in the top sediment, and net precipitation of aluminosilicate minerals below.

Our data thus suggest uptake of cations into sediments, which is most readily explained by formation of authigenic clay minerals. Our porewater and incubation data suggest that authigenic clay mineral formation is more prevalent in sediments beneath the subtropical gyre than the subpolar gyre (Figures 4 and 5), despite higher fluxes of biogenic silica to the subpolar gyre sediments (Hou et al., 2019). This is likely because silicic acid is not the only factor limiting the formation of authigenic clay minerals; aluminum and iron are also key ingredients in silicate mineral authigenesis (Dixit et al., 2001), and their aerosol supply to the subtropical gyre is greater than their supply to the subpolar gyre (Buck et al., 2013).

A survey of major element concentrations in porewaters extracted from the top 2 m of deep-sea sediments was reported for the Atlantic Ocean and Caribbean Sea (Sayles, 1979). Similar to the present study, the Atlantic survey suggested that the top meter of the sediment is a sink for potassium and bicarbonate. Contrary to the present study, the Atlantic survey suggested that the sediment is a source of calcium to the bottom water, suggested to be due to dissolution of  $\text{CaCO}_3$ . The difference between the Atlantic and North Pacific study sites is that the deep-water of the North Pacific is much more corrosive to  $\text{CaCO}_3$ :  $\Omega_{\text{calcite}}$  at 4,000 m is on average  $\sim 0.75$  along the North Pacific transect and  $\sim 1$  at  $30^\circ\text{S}$  in the Atlantic Ocean (Figure S1 in Supporting Information S1, Chung et al., 2003). Most  $\text{CaCO}_3$  dissolves before burial along the North Pacific transect and therefore little dissolution is taking place deep in the sediment. Indeed, deep-sea drilling cores from the abyssal Northeast Pacific suggest porewater calcium concentrations that are 0%–10% lower than bottom water concentrations (Manheim et al., 1970).

### 3.3. Sedimentary Evidence

The observation that potassium, strontium, and calcium are preferentially removed into sediments underneath the subtropical gyre poses a challenge since no common marine mineral is rich in all three of these elements. Energy dispersive X-ray analyses (SEM EDX) of the major element content of sediment samples from Station 2 suggest that the calcium-rich and potassium-rich phases are different; mineral grains of all sizes are potassium or calcium-rich but never contain high concentrations of both (Figures S2–S4 in Supporting Information S1). The separation between calcium- and potassium-rich phases suggests that at least two different mineral phases are forming in these sediments, one that is calcium and probably also strontium-rich, and another phase that is potassium-rich.

It is possible that the sediments underneath the subtropical gyre promote rapid reaction with seawater (time scale of months to years). For instance, small particles should be more chemically reactive than larger particles of similar mineralogy due to their large surface-to-volume ratios. Furthermore, once formed, it is likely that authigenically precipitated minerals should initially have a less well-ordered structure than detrital minerals. The hypothesis that authigenic clay minerals are forming in the sediment thus predicts the presence of small, poorly crystalline particles. To test the likelihood that part of the phases comprising abyssal North Pacific sediments are

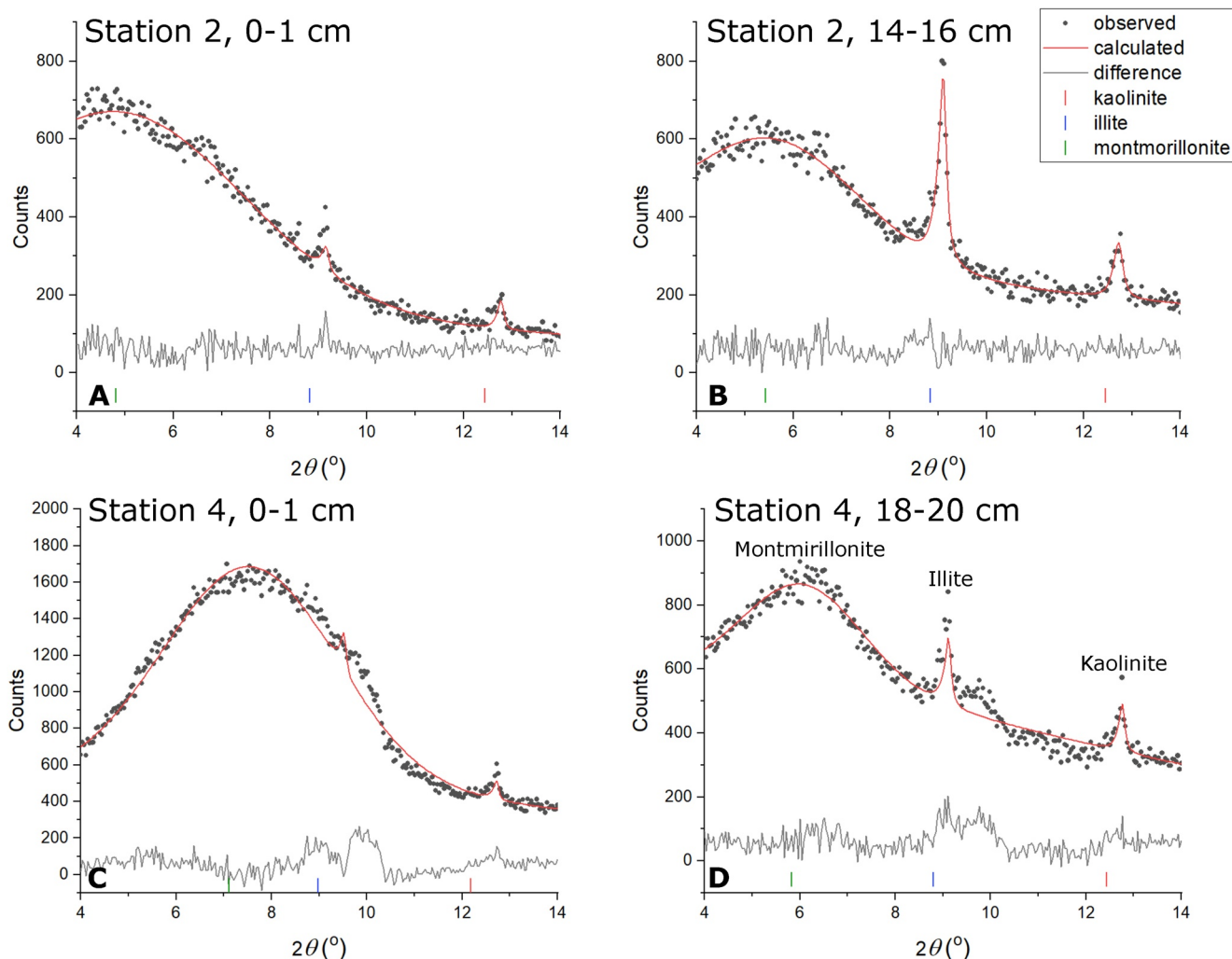


**Figure 7.** X-ray diffraction analyses of the clay fraction. Dots are the measured diffraction data, red line is the Rietveld refinement fit to the data, gray line is the absolute difference between the measurements and fit.

authigenic, we analyzed the particle size distribution at various depths in the sediment from all stations (Figure S5 in Supporting Information S1) and analyzed the XRD of the clay fraction (Figure 7).

The XRD spectra of sediment clay fractions reveal three phases with the following ideal model compositions: illite [ $K(Al_4Si_2O_9(OH)_3)$ ], kaolinite [ $Al_2Si_2O_5(OH)_4$ ], and montmorillonite-smectite [ $Ca_{0.5}(Al_2Si_4O_{11}(OH))$ ] (Figure 7). It is worth mentioning that powder diffraction is not a chemical analysis, other metals can enter the interlayer sites and this may or may not affect the observed diffraction pattern. The three clays do not share the same crystallographic properties: illite and kaolinite produce relatively sharp XRD peaks with average crystallite sizes in the tens of nm, while montmorillonite produces a much broader diffraction peak with crystallite sizes of few units of nm, going from  $1.6 \pm 0.8$  (0–1 cm specimen) to  $2.2 \pm 0.2$  nm (14–16 cm specimen) in Station 2, and from  $1.94 \pm 0.04$  (0–1 cm specimen) to  $3.2 \pm 0.2$  nm (18–20 cm specimen) in Station 4. The estimated standard deviations (e.s.d.) from the Rietveld calculation should have no bearing on the precision or accuracy, being merely related to the mathematical fit of the model (Madsen & Scarlett, 2008). In other words, absolute numbers have a degree of uncertainty that cannot be measured. On the other hand, as long as the same approach is used for all scans within a data set, the trends are reliable. The accuracy of the size determination cannot be estimated but it is reported that for a typical laboratory XRD instrument the Scherrer analysis provides sensitivity to crystallite size in the 1–100 nm range (Payzant, 2009). Therefore, the general trend is that the crystallite size of montmorillonite increases with depth in both stations, and it is relatively smaller in Station 2 compared to Station

4. The very small crystallite sizes in the core tops and increase in crystallite size with depth are consistent with gradual crystallization of montmorillonite from a partially amorphous phase.

A similar pattern of high abundance of montmorillonite in the clay fraction, producing very broad diffraction peaks, was reported for a large number of cores from the North Pacific (Griffin et al., 1968). This suggests that poorly crystalline, disordered montmorillonite is a common feature of North Pacific sediments. Oxygen isotope ratios of montmorillonite from the North Equatorial Pacific further suggest it formed at a temperature characteristic of the deep-sea (Hein et al., 1979). Since smectites as a group normally form in marine environments, wind-blown supply of montmorillonite to the ocean should be minor (Honjo et al., 1982). Sinking particulate matter collected using sediment traps at the CDisK-IV stations was rich in calcite and aragonite but its montmorillonite content was below the detection limit of the XRD analyses (Figure S6 in Supporting Information S1, Dong et al., 2019).

Cores from the subpolar gyre region are distinct from cores retrieved from the subtropical gyre region in their particle size distribution (Figure S5 in Supporting Information S1) and the high abundance of biogenic silica frustules. The geochemistry of biogenic silica test structures from Station 4 suggest that they undergo diagenetic alteration to authigenic aluminosilicate minerals (Figures S7–S9 in Supporting Information S1). Frustules from 15 cm below the sediment surface contain a considerable amount of sodium and aluminum, in addition to silicon and oxygen. The role of diagenetic enrichment of diatom frustules with aluminum and the preservation of diatom frustules was previously observed in sediments from the Amazon delta, Southern Ocean, Bering Sea, and East China Sea (Mackin & Aller, 1984; Michalopoulos & Aller, 1995; Ren et al., 2013; Van Cappellen & Qiu, 1997), pointing to the global importance of this process. Porewaters are the likely source of sodium required for recrystallization; aluminum can be leached from detrital aluminosilicates (Dixit et al., 2001; Van Cappellen & Qiu, 1997). Uptake of porewater sodium for recrystallization of biogenic shells to aluminosilicates could also be masking the signal of sedimentary Ca uptake in Ca/Na ratios from these cores and explain the discrepancy with Ca/Na and  $\delta^{44}\text{Ca}$  in the subtropical sites whereby cores from Stations 2 and 4 show a similar  $\delta^{44}\text{Ca}$  gradient but Ca/Na only decrease in cores from Stations 1–3 (Figures 5 and 6).

### 3.4. Major Element Budgets in the Abyssal Pacific and Global Ocean

Our data suggest that sediment alteration and low temperature precipitation of authigenic clay minerals could be a missing sink of calcium, strontium, and potassium in the global ocean and within their biogeochemical cycles. Sediment cores studied here span a wide geographic transect and hence can be considered to represent a substantial part of the global abyssal clay dominated seafloor. Our results suggest that potassium, strontium, and calcium fluxes into the sediments are particularly high in red clay sediments with very low sedimentation rates that receive low fluxes of biogenic and detrital material at the center of the subtropical gyre. Aluminum, silicic acid, and iron thus would be sourced from dissolution of detrital aluminosilicates (Lerman et al., 1975). Biogenic silica frustules are an excellent template for neof ormation of aluminosilicates in the subpolar gyre. The pH of the porewaters were not measured here but should play a major role in recrystallization of primary aluminosilicate minerals to secondary clays because silicate minerals are in general more soluble in basic pH solutions (Brady & Walther, 1989). In contrast to most other silicate minerals, many phyllosilicates tend to precipitate at a slightly basic pH because they contain hydroxyl ions in their structure (Tosca & Masterson, 2014). As indicated by the nitrate + nitrite profiles, more organic matter is oxidized by oxygen in the sediments underlying the subpolar gyre (Figure 2a), hence the pH of the subpolar gyre sediments is predicted to be lower (Froelich et al., 1979). A higher pH of the subtropical gyre sediments may enhance recrystallization of detrital aluminosilicates to authigenic clays. A lower pH of subpolar gyre sediments plays a double role in this context as it potentially inhibits recrystallization of detrital aluminosilicates to clays but at the same time increases the solubility of iron and aluminum oxides, and their potential to interact with biogenic silica. The initially higher proportion of clay minerals in sediments underlying the subtropical gyre is also of importance because they act as crystallization nuclei, reducing the energy barrier for precipitation of clay minerals. It should be emphasized that the data suggest recrystallization of primary aluminosilicates to clay minerals occurs at all stations and that a second process of neof ormation of aluminosilicate minerals from biogenic silica frustules is a common process in sediments of the subpolar gyre. Since the data also suggest that these new-formed minerals are sodium-rich, it is plausible that our sodium normalization of the calcium, strontium, and potassium data underestimate their fluxes in Stations 4 and 5.

Pacific Ocean red clay sediments cover an area of approximately  $9.4 \times 10^{13} \text{ m}^2$  (49% of the Pacific Ocean area, Anderson, 1988). Using the sediment-water fluxes from Table 1, a back-of-the-envelope calculation suggests sinks of calcium, strontium, and potassium into the sediment across this area on the order of  $2.6 \pm 2.4 \times 10^{12}$ ,  $1.5 \pm 0.5 \times 10^{11}$ , and  $1.4 \pm 1.0 \times 10^{13} \text{ mol y}^{-1}$ , respectively, when calculated based on the measured porewater—bottom-water concentration gradient. The calculated fluxes for calcium and strontium are around ~10% of their inputs to the global ocean, or 15% if we extrapolate to the area of red clay sediments in all ocean basins (Sun et al., 2016; Vance et al., 2009). The calculated potassium sink of  $1.4 \pm 1.0 \times 10^{13} \text{ mol y}^{-1}$  into the Pacific Ocean red clay sediments is much larger than the known inputs of potassium to the ocean. Alternatively, if we assume that the sharp decreases in calcium, strontium, and potassium concentrations observed in most cores at the sediment-bottom water interface are a sampling artifact, and calculate fluxes based only on the deeper porewater gradients, these suggest a calcium source of  $5.5 \pm 6.8 \times 10^{10}$ , a strontium sink of  $7.0 \pm 2.5 \times 10^9$ , and a potassium sink of  $1.3 \pm 0.5 \times 10^{12} \text{ mol y}^{-1}$ . Extrapolated to the global ocean, this revised flux of potassium suggests a red clay sink of  $1.9 \pm 0.7 \times 10^{12} \text{ mol y}^{-1}$ , and agrees with total global ocean inputs of potassium from rivers and hydrothermal vents of  $3 \times 10^{12} \text{ mol y}^{-1}$  (Sun et al., 2016), suggesting that authigenic clay formation in red clay dominated sediments is the main sink for potassium in the ocean. Potassium fluxes into terrigenous sediments and mid-ocean ridge basalts are higher than fluxes into red clay sediments (Sayles, 1979), but ocean margins and mid-ocean ridges occupy a smaller fraction of the global seafloor than red clays. Scaled by their relative area, potassium fluxes into terrigenous sediments and mid-ocean ridge sediments and basalts are overall smaller than fluxes into red clay sediments, and constitute most of the remaining  $1.1 \pm 0.7 \times 10^{12} \text{ mol y}^{-1}$  required to balance the global potassium budget. It is important to note, that similar to the conundrum reported by Sayles (1979), even the lowest potassium fluxes calculated based on the porewater and incubation data are higher than predicted from the potassium content of average pelagic clays. This means that uncertainties regarding the nature of the sedimentary potassium sink remain.

#### 4. Conclusions

Overall, our results highlight that the top centimeters of abyssal North Pacific sediments, typically assumed to be unreactive, are an active sink for calcium, strontium, and potassium by authigenic precipitation of clay minerals. In sediments underlying the subtropical gyre the dominant mechanism for authigenic clay precipitation is recrystallization of detrital aluminosilicates, while in subpolar sediments authigenic clay formation may be linked to alteration of biogenic silica. Relatively low net fluxes of calcium out of the sediment, and strontium into the sediment, are the result of a near balance between benthic  $\text{CaCO}_3$  dissolution and authigenic clay formation. The water column profiles from the North Pacific, which show no evidence of alkalinity increases associated with  $\text{CaCO}_3$  loss, suggest that the same applies for alkalinity, implying that authigenic clay formation in red clay sediments is an important component of the global carbon cycle.

#### Data Availability Statement

Data generated in this study are available at <https://doi.pangaea.de/10.1594/PANGAEA.946881>. The porewater and incubation data are also provided in Tables S1 and S2.

#### Acknowledgments

This study was funded by a Blavatnik postdoctoral fellowship to ZS, an Isaac Newton Trust grant to AVT and ZS, ERC StG 307582 (CARBONSINK) to AVT, and DFG Grant 458035111 to ZS. The cruise on-board RV Kilo Moana was funded by NSF Ocean Acidification Grant OCE1220600. We thank Gilad Antler for assisting with sample processing during CDisK-IV, Abby Lunstrum for analyzing particulate inorganic carbon, Christopher Jeans for discussions about clay minerals, Laura Healy for support with the particle size analyses, Harold Bradbury for support with the TIMS and Mervyn Greaves for support with the ICP-OES. Open Access funding enabled and organized by Projekt DEAL.

#### References

- Allmann, R., & Hinek, R. (2007). The introduction of structure types into the inorganic crystal structure database ICSD. *Acta Crystallographica Section A*, 63(5), 412–417. <https://doi.org/10.1107/s0108767307038081>
- Anderson, R. N. (1988). *Marine geology: A planet Earth perspective*. Wiley.
- Ayers, J. M., & Lozier, M. S. (2010). Physical controls on the seasonal migration of the North Pacific transition zone chlorophyll front. *Journal of Geophysical Research*, 115(C5), C05001. <https://doi.org/10.1029/2009jc005596>
- Baldermann, A., Warr, L. N., Letofsky-Papst, I., & Mavromatis, V. (2015). Substantial iron sequestration during green-clay authigenesis in modern deep-sea sediments. *Nature Geoscience*, 8(11), 885–889. <https://doi.org/10.1038/ngeo2542>
- Baronas, J. J., Hammond, D. E., McManus, J., Wheat, C. G., & Siebert, C. (2017). A global Ge isotope budget. *Geochimica et Cosmochimica Acta*, 203, 265–283. <https://doi.org/10.1016/j.gca.2017.01.008>
- Baronas, J. J., Hammond, D. E., Rouxel, O. J., & Monteverde, D. R. (2019). A first look at dissolved Ge isotopes in marine sediments. *Frontiers of Earth Science*, 7, 162. <https://doi.org/10.3389/feart.2019.00162>
- Berger, W. H. (1970). Biogenous deep-sea sediments: Fractionation by deep-sea circulation. *Geological Society of America Bulletin*, 81(5), 1385–1402. [https://doi.org/10.1130/0016-7606\(1970\)81\[1385:bdstfd\]2.0.co;2](https://doi.org/10.1130/0016-7606(1970)81[1385:bdstfd]2.0.co;2)
- Bernhardt, A., Oelze, M., Bouchez, J., von Blanckenburg, F., Mohtadi, M., Christl, M., & Wittmann, H. (2020).  $^{10}\text{Be}/^9\text{Be}$  ratios reveal marine authigenic clay formation. *Geophysical Research Letters*, 47(4), e2019GL086061. <https://doi.org/10.1029/2019gl086061>



- Boudreau, B. P. (1997). *Diagenetic models and their implementation*. Springer.
- Bradbury, H. J., & Turchyn, A. V. (2018). Calcium isotope fractionation in sedimentary pore fluids from ODP Leg 175: Resolving carbonate recrystallization. *Geochimica et Cosmochimica Acta*, 236, 121–139. <https://doi.org/10.1016/j.gca.2018.01.040>
- Brady, P. V., & Walther, J. V. (1989). Controls on silicate dissolution rates in neutral and basic pH solutions at 25°C. *Geochimica et Cosmochimica Acta*, 53(11), 2823–2830. [https://doi.org/10.1016/0016-7037\(89\)90160-9](https://doi.org/10.1016/0016-7037(89)90160-9)
- Brazier, J.-M., Schmitt, A.-D., Gangloff, S., Pelt, E., Chabaux, F., & Tertre, E. (2019). Calcium isotopic fractionation during adsorption onto and desorption from soil phyllosilicates (kaolinite, montmorillonite and muscovite). *Geochimica et Cosmochimica Acta*, 250, 324–347. <https://doi.org/10.1016/j.gca.2019.02.017>
- Broecker, W. S. (1971). A kinetic model for the chemical composition of sea water. *Quaternary Research*, 1(2), 188–207. [https://doi.org/10.1016/0033-5894\(71\)90041-x](https://doi.org/10.1016/0033-5894(71)90041-x)
- Broecker, W. S., & Peng, T.-H. (1982). *Tracers in the sea*. The Lamont-Doherty Geological Observatory.
- Buck, C. S., Landing, W. M., & Resing, J. (2013). Pacific Ocean aerosols: Deposition and solubility of iron, aluminum, and other trace elements. *Marine Chemistry*, 157, 117–130. <https://doi.org/10.1016/j.marchem.2013.09.005>
- Chung, S.-N., Lee, K., Feely, R. A., Sabine, C. L., Millero, F. J., Wanninkhof, R., et al. (2003). Calcium carbonate budget in the Atlantic Ocean based on water column inorganic carbon chemistry. *Global Biogeochemical Cycles*, 17(4), 1093. <https://doi.org/10.1029/2002gb002001>
- Coelho, A. (2018). TOPAS and TOPAS-Academic: An optimization program integrating computer algebra and crystallographic objects written in C++. *Journal of Applied Crystallography*, 51(1), 210–218. <https://doi.org/10.1107/s1600576718000183>
- Davis, A. C., Bickle, M. J., & Teagle, D. A. H. (2003). Imbalance in the oceanic strontium budget. *Earth and Planetary Science Letters*, 211(1–2), 173–187. [https://doi.org/10.1016/s0012-821x\(03\)00191-2](https://doi.org/10.1016/s0012-821x(03)00191-2)
- Dixit, S., Van Cappellen, P., & van Bennekom, A. J. (2001). Processes controlling solubility of biogenic silica and pore water build-up of silicic acid in marine sediments. *Marine Chemistry*, 73(3–4), 333–352. [https://doi.org/10.1016/s0304-4203\(00\)00118-3](https://doi.org/10.1016/s0304-4203(00)00118-3)
- Dong, S., Berelson, W. M., Rollins, N. E., Subhas, A. V., Naviaux, J. D., Celestian, A. J., et al. (2019). Aragonite dissolution kinetics and calcite/aragonite ratios in sinking and suspended particles in the North Pacific. *Earth and Planetary Science Letters*, 515, 1–12. <https://doi.org/10.1016/j.epsl.2019.03.016>
- Dunlea, A. G., Murray, R. W., Ramos, D. P. S., & Higgins, J. A. (2017). Cenozoic global cooling and increased seawater Mg/Ca via reduced reverse weathering. *Nature Communications*, 8(1), 844. <https://doi.org/10.1038/s41467-017-00853-5>
- Edmond, J. M., Measures, C., McDuff, R. E., Chan, L. H., Collier, R., Grant, B., et al. (1979). Ridge crest hydrothermal activity and the balances of the major and minor elements in the ocean: The Galapagos data. *Earth and Planetary Science Letters*, 46, 1–18. [https://doi.org/10.1016/0012-821x\(79\)90061-x](https://doi.org/10.1016/0012-821x(79)90061-x)
- Ehlert, C., Doering, K., Wallmann, K., Scholz, F., Sommer, S., Grasse, P., et al. (2016). Stable silicon isotope signatures of marine pore waters – Biogenic opal dissolution versus authigenic clay mineral formation. *Geochimica et Cosmochimica Acta*, 191, 102–117. <https://doi.org/10.1016/j.gca.2016.07.022>
- Emerson, S., Grundmanis, V., & Graham, D. (1982). Carbonate chemistry in marine pore waters: MANOP sites C and S. *Earth and Planetary Science Letters*, 61(2), 220–232. [https://doi.org/10.1016/0012-821x\(82\)90055-3](https://doi.org/10.1016/0012-821x(82)90055-3)
- Fantle, M. S., & Tipper, E. T. (2014). Calcium isotopes in the global biogeochemical Ca cycle: Implications for development of a Ca isotope proxy. *Earth-Science Reviews*, 129, 148–177. <https://doi.org/10.1016/j.earscirev.2013.10.004>
- Feely, R. A., Sabine, C. L., Lee, K., Millero, F. J., Lamb, M. F., Greeley, D., et al. (2002). In situ calcium carbonate dissolution in the Pacific Ocean. *Global Biogeochemical Cycles*, 16(4), 91–91-12. <https://doi.org/10.1029/2002gb001866>
- Froelich, P. N., Klinkhammer, G. P., Bender, M. L., Luedtke, N. A., Heath, G. R., Cullen, D., et al. (1979). Early oxidation of organic matter in pelagic sediments of the eastern equatorial Atlantic: Suboxic diagenesis. *Geochimica et Cosmochimica Acta*, 43(7), 1075–1090. [https://doi.org/10.1016/0016-7037\(79\)90095-4](https://doi.org/10.1016/0016-7037(79)90095-4)
- Gaboreau, S., Gailhanou, H., Blanc, P., Vieillard, P., & Made, B. (2020). Clay mineral solubility from aqueous equilibrium: Assessment of the measured thermodynamic properties. *Applied Geochemistry*, 113, 104465. <https://doi.org/10.1016/j.apgeochem.2019.104465>
- Garrels, R. M. (1965). Silica: Role in the buffering of natural waters. *Science*, 148(3666), 69. <https://doi.org/10.1126/science.148.3666.69>
- Geilert, S., Grasse, P., Doering, K., Wallmann, K., Ehlert, C., Scholz, F., et al. (2020). Impact of ambient conditions on the Si isotope fractionation in marine pore fluids during early diagenesis. *Biogeosciences*, 17(7), 1745–1763. <https://doi.org/10.5194/bg-17-1745-2020>
- Geilert, S., Grasse, P., Wallmann, K., Liebetrau, V., & Menzies, C. D. (2020). Serpentine alteration as source of high dissolved silicon and elevated  $\delta^{30}\text{Si}$  values to the marine Si cycle. *Nature Communications*, 11(1), 1–11. <https://doi.org/10.1038/s41467-020-18804-y>
- Glud, R. N., Gundersen, J. K., Jorgensen, B. B., Revsbech, N. P., & Schulz, H. D. (1994). Diffusive and total oxygen uptake of deep-sea sediments in the eastern South Atlantic Ocean: In situ and laboratory measurements. *Deep-Sea Research Part I-Oceanographic Research Papers*, 41(11–12), 1767–1788. [https://doi.org/10.1016/0967-0637\(94\)90072-8](https://doi.org/10.1016/0967-0637(94)90072-8)
- Grabowski, E., Letelier, R. M., Laws, E. A., & Karl, D. M. (2019). Coupling carbon and energy fluxes in the North Pacific subtropical gyre. *Nature Communications*, 10(1), 1895. <https://doi.org/10.1038/s41467-019-09772-z>
- Griffin, J. J., Windom, H., & Goldberg, E. D. (1968). The distribution of clay minerals in the world ocean. *Deep-Sea Research and Oceanographic Abstracts*, 15(4), 433–459. [https://doi.org/10.1016/0011-7471\(68\)90051-x](https://doi.org/10.1016/0011-7471(68)90051-x)
- Hammond, D. E., Cummins, K. M., McManus, J., Berelson, W. M., Smith, G., & Spagnoli, F. (2004). Methods for measuring benthic nutrient flux on the California Margin: Comparing shipboard core incubations to in situ lander results. *Limnology and Oceanography: Methods*, 2(6), 146–159. <https://doi.org/10.4319/lom.2004.2.146>
- Hazen, R. M., Sverjensky, D. A., Azzolini, D., Bish, D. L., Elmore, S. C., Hinnov, L., & Milliken, R. E. (2013). Clay mineral evolution. *American Mineralogist*, 98(11–12), 2007–2029. <https://doi.org/10.2138/am.2013.4425>
- Hein, J. R., Yeh, H.-W., & Alexander, E. (1979). Origin of iron-rich montmorillonite from the manganese nodule belt of the North Equatorial Pacific. *Clays and Clay Minerals*, 27(3), 185–194. <https://doi.org/10.1346/ccmn.1979.0270303>
- Hindshaw, R. S., Bourdon, B., Pogge von Strandmann, P. A. E., Vigier, N., & Burton, K. W. (2013). The stable calcium isotopic composition of rivers draining basaltic catchments in Iceland. *Earth and Planetary Science Letters*, 374, 173–184. <https://doi.org/10.1016/j.epsl.2013.05.038>
- Hindshaw, R. S., Tosca, R., Goût, T. L., Farnan, I., Tosca, N. J., & Tipper, E. T. (2019). Experimental constraints on Li isotope fractionation during clay formation. *Geochimica et Cosmochimica Acta*, 250, 219–237. <https://doi.org/10.1016/j.gca.2019.02.015>
- Honda, M. C., Imai, K., Nojiri, Y., Hoshi, F., Sugawara, T., & Kusakabe, M. (2002). The biological pump in the northwestern North Pacific based on fluxes and major components of particulate matter obtained by sediment-trap experiments (1997–2000). *Deep Sea Research Part II: Topical Studies in Oceanography*, 49(24–25), 5595–5625. [https://doi.org/10.1016/s0967-0645\(02\)00201-1](https://doi.org/10.1016/s0967-0645(02)00201-1)
- Honjo, S., Manganini, S. J., Krishfield, R. A., & Francois, R. (2008). Particulate organic carbon fluxes to the ocean interior and factors controlling the biological pump: A synthesis of global sediment trap programs since 1983. *Progress in Oceanography*, 76(3), 217–285. <https://doi.org/10.1016/j.pocean.2007.11.003>

- Honjo, S., Manganini, S. J., & Poppe, L. J. (1982). Sedimentation of lithogenic particles in the deep ocean. *Marine Geology*, 50(3), 199–220. [https://doi.org/10.1016/0025-3227\(82\)90139-6](https://doi.org/10.1016/0025-3227(82)90139-6)
- Hou, Y., Hammond, D. E., Berelson, W. M., Kemnitz, N., Adkins, J. F., & Lunstrum, A. (2019). Spatial patterns of benthic silica flux in the North Pacific reflect upper ocean production. *Deep Sea Research Part I: Oceanographic Research Papers*, 148, 25–33. <https://doi.org/10.1016/j.dsr.2019.04.013>
- IOC, SCOR, & IAPSO. (2010). *The international thermodynamic equation of seawater – 2010: Calculation and use of thermodynamic properties*, Intergovernmental Oceanographic Commission, Manuals and Guides No. 56 (p. 196). Retrieved from [www.TEOS-10.org](http://www.TEOS-10.org)
- Isson, T. T., & Planavsky, N. J. (2018). Reverse weathering as a long-term stabilizer of marine pH and planetary climate. *Nature*, 560(7719), 471–475. <https://doi.org/10.1038/s41586-018-0408-4>
- Isson, T. T., Planavsky, N. J., Coogan, L. A., Stewart, E. M., Ague, J. J., Bolton, E. W., et al. (2020). Evolution of the global carbon cycle and climate regulation on Earth. *Global Biogeochemical Cycles*, 34(2), e2018GB006061. <https://doi.org/10.1029/2018gb006061>
- Johnson, T. C. (1976). Biogenic opal preservation in pelagic sediments of a small area in the eastern tropical Pacific. *Geological Society of America Bulletin*, 87(9), 1273–1282. [https://doi.org/10.1130/0016-7606\(1976\)87<1273:bopips>2.0.co;2](https://doi.org/10.1130/0016-7606(1976)87<1273:bopips>2.0.co;2)
- Lerman, A., Mackenzie, F. T., & Bricker, O. P. (1975). Rates of dissolution of aluminosilicates in seawater. *Earth and Planetary Science Letters*, 25(1), 82–88. [https://doi.org/10.1016/0012-821x\(75\)90213-7](https://doi.org/10.1016/0012-821x(75)90213-7)
- Li, F., Penman, D., Planavsky, N. J., Knudsen, A., Zhao, M., Wang, X., et al. (2021). Reverse weathering may amplify post-Snowball atmospheric carbon dioxide levels. *Precambrian Research*, 364, 106279. <https://doi.org/10.1016/j.precamres.2021.106279>
- Li, Y. H., & Gregory, S. (1974). Diffusion of ions in sea water and in deep-sea sediments. *Geochimica et Cosmochimica Acta*, 38(5), 703–714. [https://doi.org/10.1016/0016-7037\(74\)90145-8](https://doi.org/10.1016/0016-7037(74)90145-8)
- Loucaides, S., Michalopoulos, P., Presti, M., Koning, E., Behrends, T., & Van Cappellen, P. (2010). Seawater-mediated interactions between diatomaceous silica and terrigenous sediments: Results from long-term incubation experiments. *Chemical Geology*, 270(1–4), 68–79. <https://doi.org/10.1016/j.chemgeo.2009.11.006>
- Mackenzie, F. T., & Garrels, R. M. (1966a). Chemical mass balance between rivers and oceans. *American Journal of Science*, 264(7), 507–525. <https://doi.org/10.2475/ajs.264.7.507>
- Mackenzie, F. T., & Garrels, R. M. (1966b). Silica-bicarbonate balance in the ocean and early diagenesis. *Journal of Sedimentary Research*, 36, 1075–1084. <https://doi.org/10.1306/74D715FF-2B21-11D7-8648000102C1865D>
- Mackin, J. E., & Aller, R. C. (1984). Dissolved Al in sediments and waters of the East China Sea: Implications for authigenic mineral formation. *Geochimica et Cosmochimica Acta*, 48(2), 281–297. [https://doi.org/10.1016/0016-7037\(84\)90251-5](https://doi.org/10.1016/0016-7037(84)90251-5)
- Madsen, I. C., & Scarlett, N. V. Y. (2008). Quantitative phase analysis. In R. E. Dinnebier & S. J. L. Billinge (Eds.), *Powder diffraction: Theory and practice* (pp. 298–331). Royal Society of Chemistry.
- Mangelsdorf, P. C., Wilson, T. R. S., & Daniell, E. (1969). Potassium enrichments in interstitial waters of recent marine sediments. *Science*, 165(3889), 171–174. <https://doi.org/10.1126/science.165.3889.171>
- Manheim, F., Chan, K., & Sayles, F. (1970). Interstitial water studies on small core samples, Deep Sea Drilling Project. Leg 5. *Initial Reports of the Deep Sea Drilling Project*, 5, 501–511. <https://doi.org/10.2973/dsdp.proc.5.120.1970>
- Martin, J. B., Kastner, M., & Elderfield, H. (1991). Lithium: Sources in pore fluids of Peru slope sediments and implications for oceanic fluxes. *Marine Geology*, 102(1–4), 281–292. [https://doi.org/10.1016/0025-3227\(91\)90012-s](https://doi.org/10.1016/0025-3227(91)90012-s)
- März, C., Meinhardt, A. K., Schnetger, B., & Brumsack, H. J. (2015). Silica diagenesis and benthic fluxes in the Arctic Ocean. *Marine Chemistry*, 171, 1–9. <https://doi.org/10.1016/j.marchem.2015.02.003>
- Michalopoulos, P., & Aller, R. C. (1995). Rapid clay mineral formation in Amazon delta sediments: Reverse weathering and oceanic elemental cycles. *Science*, 270(5236), 614–617. <https://doi.org/10.1126/science.270.5236.614>
- Michalopoulos, P., & Aller, R. C. (2004). Early diagenesis of biogenic silica in the Amazon delta: Alteration, authigenic clay formation, and storage. *Geochimica et Cosmochimica Acta*, 68(5), 1061–1085. <https://doi.org/10.1016/j.gca.2003.07.018>
- Middelburg, J. J., Soetaert, K., & Hagens, M. (2020). Ocean alkalinity, buffering and biogeochemical processes. *Reviews of Geophysics*, 58(3), e2019RG000681. <https://doi.org/10.1029/2019rg000681>
- Millero, F. J., Feistel, R., Wright, D. G., & McDougall, T. J. (2008). The composition of standard seawater and the definition of the reference-composition salinity scale. *Deep Sea Research Part I: Oceanographic Research Papers*, 55(1), 50–72. <https://doi.org/10.1016/j.dsr.2007.10.001>
- Milliman, J. D. (1993). Production and accumulation of calcium-carbonate in the ocean: Budget of a non steady state. *Global Biogeochemical Cycles*, 7(4), 927–957. <https://doi.org/10.1029/93gb02524>
- Ockert, C., Gussone, N., Kaufhold, S., & Teichert, B. M. A. (2013). Isotope fractionation during Ca exchange on clay minerals in a marine environment. *Geochimica et Cosmochimica Acta*, 112, 374–388. <https://doi.org/10.1016/j.gca.2012.09.041>
- Opdyke, N. D., & Foster, J. H. (1970). Paleomagnetism of cores from the North Pacific. In J. D. Hays (Ed.), *Geological investigations of the North Pacific* (p. 323). Geological Society of America.
- Payzant, E. A. (2009). Other topics. In A. Clearfield, J. H. Reibenspies, & N. Bhuvanesh (Eds.), *Principles and applications of powder diffraction* (pp. 365–380).
- Presti, M., & Michalopoulos, P. (2008). Estimating the contribution of the authigenic mineral component to the long-term reactive silica accumulation on the western shelf of the Mississippi River Delta. *Continental Shelf Research*, 28(6), 823–838. <https://doi.org/10.1016/j.csr.2007.12.015>
- Rahman, S., Aller, R. C., & Cochran, J. K. (2016). Cosmogenic <sup>32</sup>Si as a tracer of biogenic silica burial and diagenesis: Major deltaic sinks in the silica cycle. *Geophysical Research Letters*, 43(13), 7124–7132. <https://doi.org/10.1002/2016gl069929>
- Rahman, S., Aller, R. C., & Cochran, J. K. (2017). The missing silica sink: Revisiting the marine sedimentary Si cycle using cosmogenic <sup>32</sup>Si. *Global Biogeochemical Cycles*, 31(10), 1559–1578. <https://doi.org/10.1002/2017gb005746>
- Ren, H., Brunelle, B. G., Sigman, D. M., & Robinson, R. S. (2013). Diagenetic aluminum uptake into diatom frustules and the preservation of diatom-bound organic nitrogen. *Marine Chemistry*, 155, 92–101. <https://doi.org/10.1016/j.marchem.2013.05.016>
- Ridgwell, A., & Zeebe, R. E. (2005). The role of the global carbonate cycle in the regulation and evolution of the Earth system. *Earth and Planetary Science Letters*, 234(3–4), 299–315. <https://doi.org/10.1016/j.epsl.2005.03.006>
- Santiago Ramos, D. P., Coogan, L. A., Murphy, J. G., & Higgins, J. A. (2020). Low-temperature oceanic crust alteration and the isotopic budgets of potassium and magnesium in seawater. *Earth and Planetary Science Letters*, 541, 116290. <https://doi.org/10.1016/j.epsl.2020.116290>
- Sayles, F. L. (1979). The composition and diagenesis of interstitial solutions-1. Fluxes across the seawater-sediment interface in the Atlantic Ocean. *Geochimica et Cosmochimica Acta*, 43(4), 527–545. [https://doi.org/10.1016/0016-7037\(79\)90163-7](https://doi.org/10.1016/0016-7037(79)90163-7)
- Sayles, F. L., & Bischoff, J. L. (1973). Ferromanganoan sediments in the equatorial East Pacific. *Earth and Planetary Science Letters*, 19(3), 330–336. [https://doi.org/10.1016/0012-821x\(73\)90083-6](https://doi.org/10.1016/0012-821x(73)90083-6)
- Schlitzer, R. (2020). Ocean Data View.

- Schrag, D. P. (1999). Rapid analysis of high-precision Sr/Ca ratios in corals and other marine carbonates. *Paleoceanography*, *14*(2), 97–102. <https://doi.org/10.1029/1998pa900025>
- Schrum, H. N., Murray, R. W., & Gribsholt, B. (2012). Comparison of Rhizon sampling and whole round squeezing for marine sediment porewater. *Scientific Drilling*, *13*, 47–50. <https://doi.org/10.5194/sd-13-47-2012>
- Siever, R. (1992). The silica cycle in the Precambrian. *Geochimica et Cosmochimica Acta*, *56*(8), 3265–3272. [https://doi.org/10.1016/0016-7037\(92\)90303-z](https://doi.org/10.1016/0016-7037(92)90303-z)
- Sillén, L. G. (1967). The ocean as a chemical system. *Science*, *156*(3779), 1189–1197. <https://doi.org/10.1126/science.156.3779.1189>
- Soetaert, K., Hofmann, A. F., Middelburg, J. J., Meysman, F. J. R., & Greenwood, J. (2007). The effect of biogeochemical processes on pH. *Marine Chemistry*, *105*(1–2), 30–51. <https://doi.org/10.1016/j.marchem.2006.12.012>
- Staudigel, H., Hart, S. R., & Richardson, S. H. (1981). Alteration of the oceanic crust: Processes and timing. *Earth and Planetary Science Letters*, *52*(2), 311–327. [https://doi.org/10.1016/0012-821x\(81\)90186-2](https://doi.org/10.1016/0012-821x(81)90186-2)
- Steiner, Z., Lazar, B., Erez, J., & Turchyn, A. V. (2018). Comparing Rhizon samplers and centrifugation for pore-water separation in studies of the marine carbonate system in sediments. *Limnology and Oceanography: Methods*, *16*(12), 828–839. <https://doi.org/10.1002/lom3.10286>
- Steiner, Z., Sarkar, A., Liu, X., Berelson, W. M., Adkins, J. F., Prabhakaran, S., et al. (2021). On calcium-to-alkalinity anomalies in the North Pacific, Red Sea, Indian Ocean and Southern Ocean. *Geochimica et Cosmochimica Acta*, *303*, 1–14. <https://doi.org/10.1016/j.gca.2021.03.027>
- Steiner, Z., Sarkar, A., Prakash, S., Vinayachandran, P. N., & Turchyn, A. V. (2020). Dissolved strontium, Sr/Ca ratios, and the abundance of Acantharia in the Indian and Southern Oceans. *ACS Earth Space Chemistry*, *4*(6), 802–811. <https://doi.org/10.1021/acsearthspacechem.9b00281>
- Subhas, A. V., Adkins, J. F., Dong, S., Rollins, N. E., & Berelson, W. M. (2020). The carbonic anhydrase activity of sinking and suspended particles in the North Pacific Ocean. *Limnology and Oceanography*, *65*(3), 637–651. <https://doi.org/10.1002/lno.11332>
- Subhas, A. V., Dong, S., Naviaux, J. D., Rollins, N. E., Ziveri, P., Gray, W., et al. (2022). Shallow calcium carbonate cycling in the North Pacific Ocean. *Global Biogeochemical Cycles*, *36*(5), e2022GB007388. <https://doi.org/10.1029/2022gb007388>
- Sulpis, O., Boudreau, B. P., Mucci, A., Jenkins, C., Trossman, D. S., Arbic, B. K., & Key, R. M. (2018). Current CaCO<sub>3</sub> dissolution at the seafloor caused by anthropogenic CO<sub>2</sub>. *Proceedings of the National Academy of Sciences of the United States of America*, *115*(46), 11700–11705. <https://doi.org/10.1073/pnas.1804250115>
- Sun, X. L., Higgins, J., & Turchyn, A. V. (2016). Diffusive cation fluxes in deep-sea sediments and insight into the global geochemical cycles of calcium, magnesium, sodium and potassium. *Marine Geology*, *373*, 64–77. <https://doi.org/10.1016/j.margeo.2015.12.011>
- Taylor, B. J., Rae, J. W. B., Gray, W. R., Darling, K. F., Burke, A., Gersonde, R., et al. (2018). Distribution and ecology of planktic foraminifera in the North Pacific: Implications for paleo-reconstructions. *Quaternary Science Reviews*, *191*, 256–274. <https://doi.org/10.1016/j.quascirev.2018.05.006>
- Timothy, D. A., Wong, C. S., Barwell-Clarke, J. E., Page, J. S., White, L. A., & Macdonald, R. W. (2013). Climatology of sediment flux and composition in the subarctic Northeast Pacific Ocean with biogeochemical implications. *Progress in Oceanography*, *116*, 95–129. <https://doi.org/10.1016/j.pocan.2013.06.017>
- Tipper, E. T., Gaillardet, J., Galy, A., Louvat, P., Bickle, M. J., & Capmas, F. (2010). Calcium isotope ratios in the world's largest rivers: A constraint on the maximum imbalance of oceanic calcium fluxes. *Global Biogeochemical Cycles*, *24*(3), 13. <https://doi.org/10.1029/2009gb003574>
- Tosca, N. J., & Masterson, A. L. (2014). Chemical controls on incipient Mg-silicate crystallization at 25°C: Implications for early and late diagenesis. *Clay Minerals*, *49*(2), 165–194. <https://doi.org/10.1180/claymin.2014.049.2.03>
- Van Cappellen, P., & Qiu, L. (1997). Biogenic silica dissolution in sediments of the Southern Ocean. I. Solubility. *Deep Sea Research Part II: Topical Studies in Oceanography*, *44*(5), 1109–1128. [https://doi.org/10.1016/s0967-0645\(96\)00113-0](https://doi.org/10.1016/s0967-0645(96)00113-0)
- Vance, D., Teagle, D. A. H., & Foster, G. L. (2009). Variable Quaternary chemical weathering fluxes and imbalances in marine geochemical budgets. *Nature*, *458*(7237), 493–496. <https://doi.org/10.1038/nature07828>
- Wurgaft, E., Steiner, Z., Luz, B., & Lazar, B. (2016). Evidence for inorganic precipitation of CaCO<sub>3</sub> on suspended solids in the open water of the Red-Sea. *Marine Chemistry*, *186*, 145–155. <https://doi.org/10.1016/j.marchem.2016.09.006>
- Zhang, X. Y., Gaillardet, J., Barrier, L., & Bouchez, J. (2022). Li and Si isotopes reveal authigenic clay formation in a palaeo-delta. *Earth and Planetary Science Letters*, *578*, 117339. <https://doi.org/10.1016/j.epsl.2021.117339>

## References From the Supporting Information

- Naviaux, J. D., Subhas, A. V., Rollins, N. E., Dong, S., Berelson, W. M., & Adkins, J. F. (2019). Temperature dependence of calcite dissolution kinetics in seawater. *Geochimica et Cosmochimica Acta*, *246*, 363–384. <https://doi.org/10.1016/j.gca.2018.11.037>